Spin-singlet ground state with spin gap in $S_{\rm eff} = 1/2$ antiferromagnetic tetramer compound Yb_2SiO_5

Masashi Hase[1],* Koji Kaneko[2,3], Chihiro Tabata[2,3],
Hiroki Yamauchi[2,3], Naohito Tsujii[1], and Andreas Dönni[1]

[1]*Research Center for Materials Nanoarchitectonics (MANA), National Institute for Materials Science (NIMS), 1-2-1 Sengen, Tsukuba, Ibaraki 305-0047, Japan*

[2]*Materials Science Research Center, Japan Atomic Energy Agency (JAEA), 2-4 Shirakata, Tokai, Naka, Ibaraki 319-1195, Japan*

[3]*Advanced Science Research Center, Japan Atomic Energy Agency (JAEA), 2-4 Shirakata, Tokai, Naka, Ibaraki 319-1195, Japan*

(Dated: January 17, 2025)

Abstract

We studied the magnetic properties of Yb_2SiO_5 with pseudospins of $S_{\rm eff} = 1/2$ using magnetic susceptibility, specific heat, and inelastic neutron scattering (INS) measurements. A broad maximum appears at $T_{\rm max} \sim 6$ K in the plot of the magnetic susceptibility $[\chi(T)]$ as a function of temperature (T), indicating a low-dimensional antiferromagnetic (AFM) spin system. The susceptibility decreases rapidly with decreasing T below $T_{\rm max}$, suggesting a spin-singlet ground state with a spin gap. We observed cluster-like excitations for energy transfers of $\omega \sim 0.7, 1.2$, and 1.9 meV in the INS measurements. The T dependence of the intensity $[I(T)]$ indicates that the three excitations are magnetic ones. We determined that the spin system in Yb_2SiO_5 is the $S_{\rm eff} = 1/2$ AFM tetramer with two exchange interactions of $J_1 = 0.74$ meV and $J_2 = 0.95$ meV. The isolated spin tetramer model can explain the excitation energies, $\chi(T)$, magnetic specific heat at $T < 15$ K, and the magnitude of the scattering vector (Q) dependence of the intensity $[I(Q)]$ at 0.7 and 1.2 meV. This model, however, cannot well explain the $I(Q)$ at 1.9 meV and the $I(T)$ of the three excitations, likely because of the effects of weak inter-tetramer interactions.

PACS numbers:

*Electronic address: HASE.Masashi@nims.go.jp

I. INTRODUCTION

A spin system determined using inelastic neutron scattering (INS) experiments is sometimes different from that expected from a crystal structure. For example, $(VO)_2P_2O_7$ was considered to have a two-leg antiferromagnetic (AFM) Heisenberg spin ladder with chains running in the crystallographic a direction [1]. Dispersion relations of magnetic excitations were obtained from INS experiments on a single crystal [2]. The results indicate that $(VO)_2P_2O_7$ is best described as an AFM alternating spin chain directed along the b direction. In $CuWO_4$, short Cu-Cu pairs form an alternating spin chain running in the b direction [3], whereas the INS results on a single crystal show that an AFM alternating spin chain runs in the $[2, -1, 0]$ direction [4].

We can determine s spin system from the Q dependence of the INS intensity $[I(Q)]$ of a powder sample. For example, $CaCuGe_2O_6$ has a spin-singlet ground state (GS) with a spin gap [5]. The first- and second-nearest neighbor (1NN and 2NN) Cu–Cu pairs with the Cu–Cu lengths of 3.072 and 5.213 Å, respectively [6], can form a frustrated spin chain if the 2NN exchange interaction is AFM. A spin-singlet GS with a spin gap is possible in the frustrated spin chain [7–10]. The magnetic susceptibility, however, can be explained well by an isolated AFM spin dimer [5]. Therefore, it was inferred that the exchange interaction in the third-nearest neighbor Cu–Cu pair (5.549 Å) is dominant and form the AFM spin dimer. The inference was proved to be correct by $I(Q)$ of the powder sample [11]. In $VODPO_4 - \frac{1}{2}D_2O$, the $I(Q)$ result showed that the origin of the spin-singlet GS with the spin gap is the AFM spin dimer with the V–V length of 4.43 Å instead of the dimer with the V–V length of 3.09 Å [12]. In β-$AgCuPO_4$, the 1NN and 2NN Cu–Cu pairs (3.10 and 3.37 Å, respectively) form a distorted honeycomb lattice [13]. According to the prediction based on spin-dimer analysis [14], however, a long Cu–Cu pair (5.20 Å) has the strongest exchange interaction and two strong interactions form an AFM alternating spin chain. The INS results on the powder sample proved that this prediction is correct [15].

To increase the evidence that the method to determine a spin system from $I(Q)$ of a powder sample is useful, we are paying attention to Yb^{3+}-based substances because various spin systems described below have been found. A spin system that cannot be uniquely determined from a crystal structure must exist in Yb^{3+}-based substances. In a Yb^{3+} ($J = 7/2$) ion with low point symmetry, the ground-state multiplet is split into four Kramers

doublets by crystalline electric fields (CEFs). Here, J denotes the magnitude of the total angular momentum. It is considered that a Yb^{3+} ion at low temperatures has pseudospin of 1/2 ($S_{\rm eff} = 1/2$) at a Kramers doublet with the lowest energy if the energy separation between the lowest and second-lowest Kramers doublets are larger than the temperatures. Examples of various spin systems are a spin chain in $NaYbTe_2O_7$ [16] and $YbAlO_3$ [17], a triangular lattice in $YbMgGaO_4$ [18–20], $YbZnGaO_4$ [21], $YbBO_3$ [22], and $NaYbO_2$ [23], a honeycomb lattice in YbOCl [24] and $YbCl_3$ [25, 26], a distorted honeycomb lattice in $Yb_2Si_2O_7$ [27] and $BiYbGeO_5$ [28], a breathing pyrochlore lattice in $Ba_3Yb_2Zn_5O_{11}$ [29], a Shastry–Sutherland lattice in $Yb_2Be_2GeO_7$ [30], and a hyperkagome lattice in $Li_3Yb_3Te_2O_{12}$ [31] and $Yb_3Sc_2Ga_3O_{12}$ [32].

To find an intriguing spin system in Yb^{3+}-based substances, we have been focusing on Yb_2SiO_5 in this study. Figures 1(a) and (b) show the crystal structure. The space group is monoclinic $C2/c$ (No. 15) [33–35]. The lattice constants at room temperature are $a = 14.28, b = 6.653, c = 10.28$ Å, and $\beta = 122.2°$ [34]. Distorted tetrahedra of SiO_4 and distorted octahedra of YbO_6 are formed. Figures 1(c) and (d) depict the positions of Yb^{3+} ions [33–35]. There are two crystallographic Yb^{3+}-ion sites (Yb1 and Yb2); they are indicated by red and blue circles, respectively. Both of the Yb^{3+} sites are $8f$ sites, and the site symmetry is 1, meaning that no point symmetry exists. Thus, pseudospins with $S_{\rm eff} = 1/2$ can be realized. The first- to fifth-nearest neighbor (1NN to 5NN) Yb–Yb pairs have two Yb–O–Yb paths. The five types of Yb–Yb pairs are represented by bars in Fig. 1, and the Yb–Yb lengths and Yb–O–Yb angles are reported in Table I. We expected that the four exchange interactions except for the 4NN interaction formed a two-leg spin ladder with chains running in the c direction as surrounded by the dashed rectangle. Two-leg spin ladders are connected by the 4NN interaction (3.571 Å). The magnetic properties of Yb_2SiO_5 have not been reported and it is not determined which Yb–Yb pairs have dominant exchange interactions. Accordingly, we investigated the magnetic properties of Yb_2SiO_5 using magnetic susceptibility, specific heat, and INS measurements.

II. EXPERIMENTAL METHODS

We synthesized crystalline powders of Yb_2SiO_5 and nonmagnetic Lu_2SiO_5 via a solid-state reaction. The starting materials were Yb_2O_3, Lu_2O_3, and SiO_2 powders with 99.95 %,

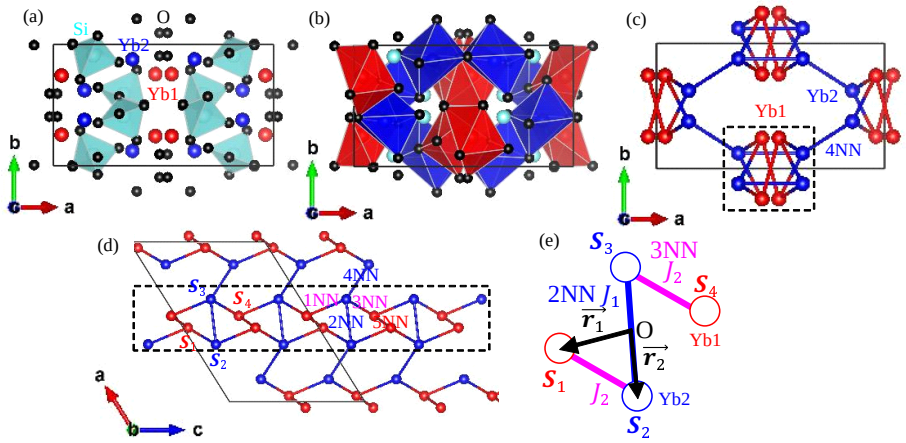

FIG. 1: (a)(b) The crystal structure of Yb_2SiO_5, as drawn using VESTA [36]. The solid rectangle represents the unit cell. Red, blue, light-blue, and black circles denote Yb1, Yb2, Si, and O sites. Distorted tetrahedra of SiO_4 and distorted octahedra of YbO_6 are also shown. (c)(d) Schematic showing the positions of Yb^{3+} ions. The solid rectangle in (c) and parallelogram in (d) represent the unit cell. The five types of Yb–Yb pairs that have two Yb–O–Yb paths are represented by bars. 1NN, 2NN, 3NN, 4NN, and 5NN denote the first-, second-, third-, fourth-, and fifth-nearest neighbor Yb–Yb pairs, respectively. As indicated by the dashed rectangle, a two-leg spin ladder with chains running in the c direction are formed by the four exchange interactions except for the 4NN interaction. Two-leg spin ladders are connected by the 4NN interaction. (e) The actual spin system (spin tetramer) formed by 2NN and 3NN Yb–Yb pairs indicated by blue and pink lines, respectively. The Hamiltonian is expressed as $\mathcal{H} = J_2(\boldsymbol{S}_1 \cdot \boldsymbol{S}_2 + \boldsymbol{S}_3 \cdot \boldsymbol{S}_4) + J_1 \boldsymbol{S}_2 \cdot \boldsymbol{S}_3$. The positions of $\boldsymbol{S}_1$ and $\boldsymbol{S}_2$ are denoted by $\vec{r_1}$ and $\vec{r_2}$, respectively, where the origin is the center of two Yb2 sites.

99.9 %, and 99.9 % purities, respectively. A stoichiometric mixture of the powders was sintered in air at 1523 K for Yb_2SiO_5 or 1573 K for Lu_2SiO_5 with intermediate grinding. X-ray powder diffraction patterns were recorded at room temperature using an X-ray diffractometer (RINT-TTR III; Rigaku). Within the experimental accuracy, the obtained samples were single-phase. The lattice constants evaluated by us are almost the same as those in [34].

We measured the magnetic susceptibility and specific heat using a Quantum Design magnetic property measurement system and a Quantum Design Dynacool, respectively. We performed INS measurements using the low-energy triple-axis spectrometer (LTAS) installed at the JRR-3 reactor at the Japan Atomic Energy Agency (JAEA). The energy of the final

TABLE I: Yb–Yb length and Yb–O–Yb angle in the first- to fifth-nearest neighbor (1NN to 5NN) Yb–Yb pairs [34]. Yb1 and Yb2 sites are surrounded by six O^{2-} ions with Yb–O lengths of 2.183–2.339 Å and 2.167–2.260 Å, respectively.

		Yb-Yb (Å)	Yb-O-Yb (degrees)	
1NN	Yb1-Yb2	3.358	95.66	98.17
2NN	Yb2-Yb2	3.431	101.56 ×2	
3NN	Yb1-Yb2	3.477	99.21	100.92
4NN	Yb2-Yb2	3.571	105.55 ×2	
5NN	Yb1-Yb1	3.599	105.42 ×2	

neutrons was fixed at 2.6 meV. Higher-order beam contamination was effectively eliminated using a cooled Be filter positioned in front of the sample. The energy resolution was 0.1 meV (full-width at half-maximum, FWHM) for an energy transfer of $\omega = 0$ meV. The resolution was determined from incoherent scattering from the sample. A powder sample of approximately 8.7 g was mounted in a top-load cryostat [37].

III. RESULTS

The red circles in Fig. 2 show the temperature (T) dependence of the magnetic susceptibility [$\chi(T)$] of Yb_2SiO_5 powder measured in a magnetic field of $\mu_0 H = 0.01$ T. A broad maximum is observed at $T_{\rm max} \sim 6$ K [Fig. 2(a)], indicating a low-dimensional AFM spin system. The susceptibility decreases rapidly with decreasing T at temperatures less than $T_{\rm max}$, suggesting a spin-singlet GS with a spin gap. A spin-singlet GS with a spin gap appears in $Yb_2Si_2O_7$ (AFM dimer) [27], $BiYbGeO_5$ (AFM dimer) [28], and $Ba_3Yb_2Zn_5O_{11}$ (AFM tetrahedron) [29]. The calculated $\chi(T)$ values indicated by lines will be explained later.

Red and blue circles in Fig. 3(a) show the T dependence of the magnetic specific heat $C_{\rm mag}(T)$ of Yb_2SiO_5 powder under 0 and 9 T magnetic fields, respectively. The magnetic specific heat was obtained by subtracting the specific heat of nonmagnetic isostructural Lu_2SiO_5 at 0 T from that of Yb_2SiO_5. A maximum of $C_{\rm mag}(T)$ is observed at approximately 4 and 8 K in the data recorded under 0 and 9 T fields, respectively. No transition appears at $T \geq 2$ K and $\mu_0 H \leq 14$ T. The calculated $C_{\rm mag}(T)$ indicated by lines will be explained

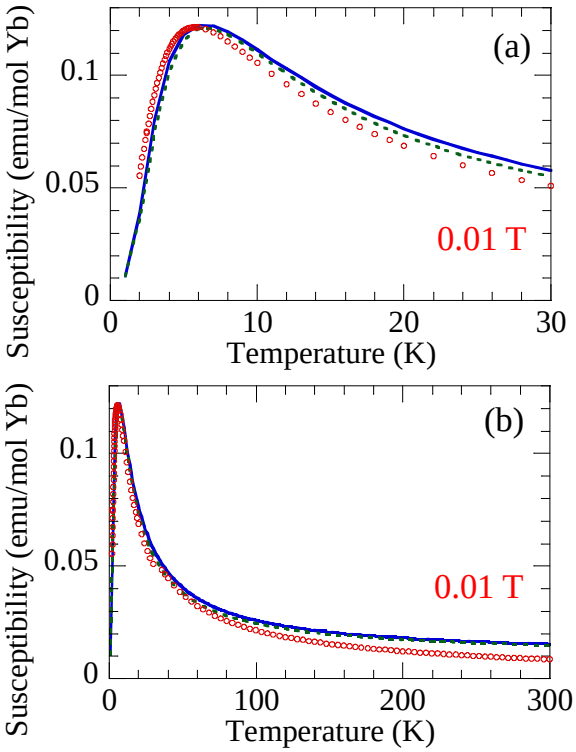

FIG. 2: The T dependence of the magnetic susceptibility $\chi(T)$ of Yb_2SiO_5 powder under a 0.01 T magnetic field (circles). The solid line indicates $\chi(T)$ values calculated for the spin-1/2 tetramer with $J_1 = 0.74$ meV, $J_2 = 0.95$ meV, $g = 4.2$, and a constant term $\chi_0 = 0.01$ (emu/mol Yb). The dashed line indicates the sum of $\chi(T)$ values calculated for two isolated spin-1/2 dimers with the exchange interactions of 0.7 and 1.2 meV. We used $g = 4.0$ and a constant term $\chi_0 = 0.01$ (emu/mol Yb) for the $\chi(T)$ values.

later. Figure 3(b) shows the magnetic entropy $S_{\rm mag}(T)$ of Yb_2SiO_5. The value of entropy reaches $R\ln 2$ and $R\ln 4$ at $T \sim 23$ and ~ 150 K, respectively.

Figure 4 shows the INS intensity $I(Q,\omega)$ map of Yb_2SiO_5 powder at 1.8 K, where Q and ω are the magnitude of the scattering vector and the energy transfer, respectively. We observed excitations at $\omega \sim 0.7, 1.2$, and 1.9 meV. The excitations are dispersionless and exist over a wide Q range, indicating cluster excitations.

Figure 5(a) depicts the ω dependence of the INS intensity $I(\omega)$ of Yb_2SiO_5 powder at the four investigated temperatures. The line shows the sum of three Gaussians each with a FWHM of 0.1 meV, which was evaluated from the incoherent scattering. The three peaks

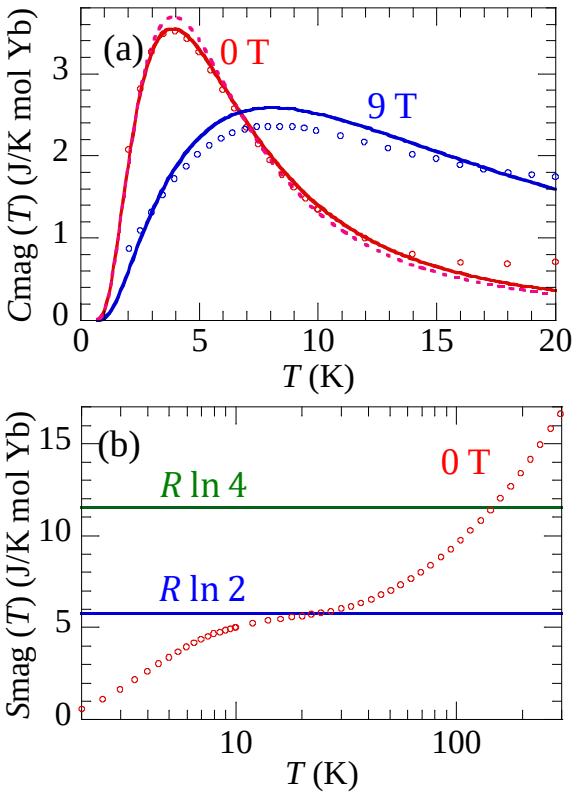

FIG. 3: (a) The T dependence of the magnetic specific heat $C_{\rm mag}(T)$ of Yb_2SiO_5 under 0 and 9 T magnetic fields (circles). The solid lines indicate $C_{\rm mag}(T)$ values calculated for the spin-1/2 tetramer with $J_1 = 0.74$ meV, $J_2 = 0.95$ meV, and $g = 4.2$ for the 9 T data. The dashed line indicates the sum of $C_{\rm mag}(T)$ values at 0 T calculated for two isolated spin-1/2 dimers with the exchange interactions of 0.7 and 1.2 meV. (b) The T dependence of the magnetic entropy $S_{\rm mag}(T)$ of Yb_2SiO_5 under a 0 T magnetic field.

are slightly wider than the resolution, consistent with the picture of the cluster excitations. Figure 5(b) represents the T dependence of the integrated intensity $I(T)$ of the 0.7, 1.2, and 1.9 meV excitations. As T is raised, the intensities of the 0.7 and 1.2 meV excitations decrease at $T \leq 30$ K and are almost constant at $T \geq 30$ K. The 1.9 meV excitation is observed only at low temperatures. The T dependence indicates that the three excitations are magnetic in nature. The peak positions are almost independent of T. The calculated $I(T)$ values indicated by the lines will be explained later.

Figure 6 shows the Q dependence of the INS intensity $I(Q)$ at $\omega = 0.7, 1.2$, and 1.9

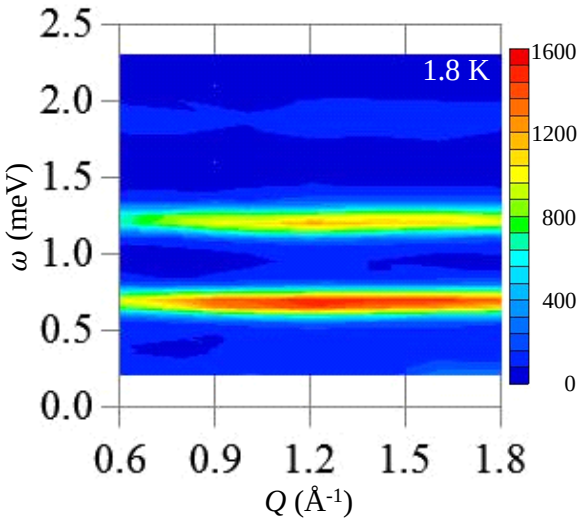

FIG. 4: The INS intensity $I(Q,\omega)$ map of Yb_2SiO_5 powder at 1.8 K. The energy of the final neutrons is 2.6 meV. The vertical key on the right shows the INS intensity in arbitrary units.

meV. A broad maximum is observed at $Q \sim 1.25$ Å^{-1} in the three experimental curves, although the Q dependence of the INS intensity is weak at the 1.9 meV excitation. As shown in Fig. 6(b), $I(Q)$ at $\omega = 1.9$ meV cannot be explained by the square of the magnetic form factor $[f(Q)^2]$ of Yb^{3+} ions [38]. The experimental Q dependence indicates that the three excitations are not CEF excitations of Yb^{3+} ions because the intensity of the CEF excitations decreases monotonically with increasing Q as $f(Q)^2$. The calculated $I(Q)$ values indicated by the solid lines will be explained later.

IV. ANALYSES AND DISCUSSION

We consider a spin system that can explain the experimental results for Yb_2SiO_5. The spin system is a spin cluster because the magnetic excitations are dispersionless. The simplest cluster is an AFM dimer. As is shown in Fig. 1 and Table I, two types of $S_{\rm eff} = \frac{1}{2}$ AFM dimers are possible: Yb1–Yb1 and Yb2–Yb2 dimers can be formed by the 5NN Yb–Yb pair and the 2NN or 4NN pair, respectively. In this case for two isolated dimers, two spin-gap excitations appear. Thus, the three magnetic excitations cannot be explained.

Even if the weak 1.9 meV excitation is ignored, any spin model formed by two types of AFM dimers cannot explain the difference in the intensity between the 0.7 and 1.2 meV

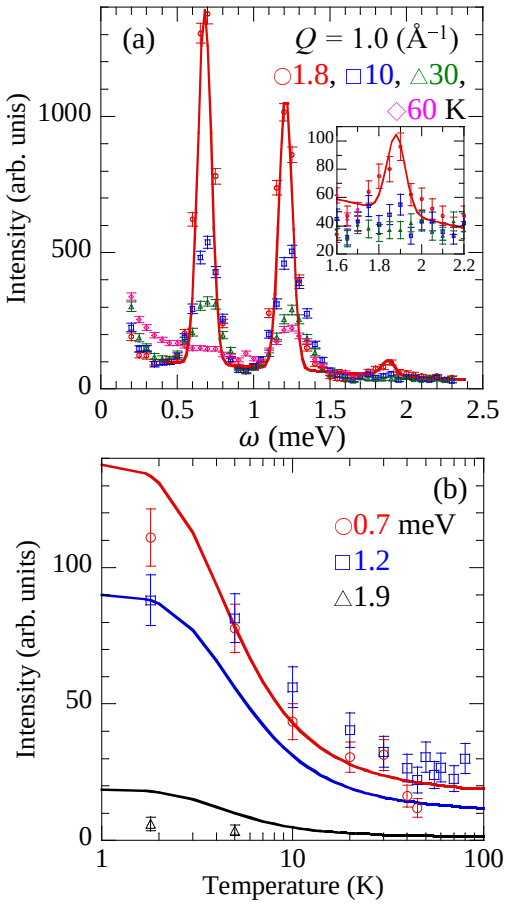

FIG. 5: (a) The ω dependence of the INS intensity $I(\omega)$ of Yb_2SiO_5 powder at $Q = 1.0$ Å^{-1} and various temperatures. The energy of the final neutrons is 2.6 meV. The line shows the sum of three Gaussians each with a FWHM of 0.1 meV. The inset is an enlarged figure clearly showing the 1.9 meV excitation. (b) The T dependence of the integrated intensity of the 0.7, 1.2, and 1.9 meV excitations. The red, blue, and black lines indicate the integrated intensity of the excitations from GS ($|02\rangle$) to 1ES ($|13\rangle$), 2ES ($|11\rangle$), and 4ES ($|12\rangle$), respectively, calculated for the spin-1/2 tetramer with $J_1 = 0.74$ meV and $J_2 = 0.95$ meV. The three lines are multiplied by the same value.

excitations. The powder-averaged INS intensity at the dimer-gap energy is given by [11]

$$I(Q) = r_0^2 \frac{k'}{k} Npf(Q)^2 (1 - \frac{\sin(2Qd)}{2Qd}). \quad (1)$$

Here, k and k' are the incident and scattered neutron wave numbers, respectively, and $r_0 = -0.54 \times 10^{-12}$ cm. The parameters N, p, $f(Q)$, and $2d$ denote the number of dimers, the thermal population factor for the ground state [39], the magnetic form factor of Yb^{3+}

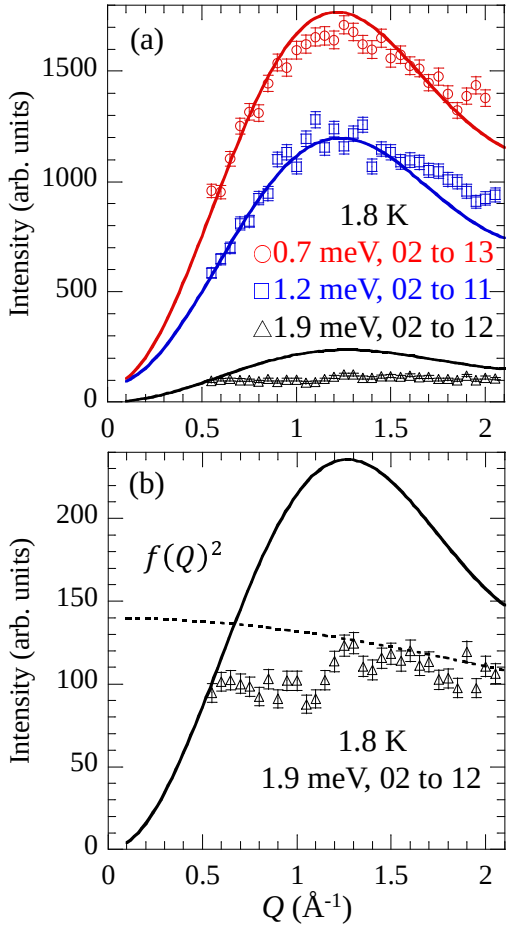

FIG. 6: (a) The Q dependence of the INS intensity $I(Q)$ at 1.8 K for Yb_2SiO_5 powder at 0.7, 1.2, and 1.9 meV. The red, blue, and black lines indicate $I(Q)$ for the excitations from GS ($|02\rangle$) to 1ES ($|13\rangle$), 2ES ($|11\rangle$), and 4ES ($|12\rangle$), respectively, calculated for the spin-1/2 tetramer formed by 3NN and 2NN Yb–Yb pairs with $J_1 = 0.74$ meV and $J_2 = 0.95$ meV. The three lines are multiplied by the same value. (b) Enlarged figure of (a) for the 1.9 meV excitation. The square of the magnetic form factor of a Yb^{3+} ion is shown by the dashed line.

ions, and the Yb–Yb length in a dimer, respectively. We measured the INS intensity using the fixed final energy (2.6 meV) and a fixed beam monitor. The value of k'/k was then already accounted for. The difference in intensity between the 0.7 and 1.2 meV excitations is generated by $\frac{k'}{k}$, p, and $2d$. The values of $\frac{k'}{k}$ and p at 1.8 K were calculated to be 0.888 and 0.968, respectively, for the 0.7 meV excitation and 0.827 and 0.999, respectively, for the 1.2 meV excitation. Thus, $\frac{k'}{k}p$ is 0.860 and 0.827 for the 0.7 and 1.2 meV excitations,

TABLE II: Yb–Yb length in six tetramers formed by two types of Yb–Yb pairs. As shown in Fig. 1(c), $|\vec{r_1} - \vec{r_2}|$, $|2\vec{r_2}|$, $|\vec{r_1} + \vec{r_2}|$, and $|2\vec{r_1}|$ correspond to the lengths between $\boldsymbol{S}_1$ and $\boldsymbol{S}_2$ (also $\boldsymbol{S}_3$ and $\boldsymbol{S}_4$), between $\boldsymbol{S}_2$ and $\boldsymbol{S}_3$, between $\boldsymbol{S}_1$ and $\boldsymbol{S}_3$ (also $\boldsymbol{S}_2$ and $\boldsymbol{S}_4$), and between $\boldsymbol{S}_1$ and $\boldsymbol{S}_4$, respectively.

tetramer		$\lvert\vec{r_1} - \vec{r_2}\rvert$ (Å)	$\lvert 2\vec{r_2}\rvert$ (Å)	$\lvert\vec{r_1} + \vec{r_2}\rvert$ (Å)	$\lvert 2\vec{r_1}\rvert$ (Å)
		$\boldsymbol{S}_1$ and $\boldsymbol{S}_2$	$\boldsymbol{S}_2$ and $\boldsymbol{S}_3$	$\boldsymbol{S}_1$ and $\boldsymbol{S}_3$	$\boldsymbol{S}_1$ and $\boldsymbol{S}_4$
		$\boldsymbol{S}_3$ and $\boldsymbol{S}_4$		$\boldsymbol{S}_2$ and $\boldsymbol{S}_4$	
1NN-2NN	Yb1-Yb2-Yb2-Yb1	3.357	3.431	4.096	6.458
1NN-4NN	Yb1-Yb2-Yb2-Yb1	3.357	3.571	6.183	9.287
1NN-5NN	Yb2-Yb1-Yb1-Yb2	3.357	3.599	3.696	6.077
3NN-2NN	Yb1-Yb2-Yb2-Yb1	3.477	3.431	3.696	3.986
3NN-4NN	Yb1-Yb2-Yb2-Yb1	3.477	3.571	5.693	8.732
3NN-5NN	Yb2-Yb1-Yb1-Yb2	3.477	3.599	4.096	6.692

respectively. As shown in Table I, the values of $2d$ for Yb1–Yb1 and Yb2–Yb2 dimers are close to each other. Consequently, the intensities of the 0.7 and 1.2 meV excitations must be similar to each other, which is inconsistent with the $I(Q)$ results in Fig. 6.

The next simplest cluster that has a spin-singlet ground state is a tetramer (four-spin system). When we select two types of Yb–Yb pairs in Table I, six types of spin tetramers are possible, as listed in Table II. In any tetramer, the Hamiltonian is expressed as

$$\mathcal{H} = J_2(\boldsymbol{S}_1 \cdot \boldsymbol{S}_2 + \boldsymbol{S}_3 \cdot \boldsymbol{S}_4) + J_1 \boldsymbol{S}_2 \cdot \boldsymbol{S}_3. \tag{2}$$

There are two $S^{\mathrm{T}} = 0$ states ($|01\rangle$ and $|02\rangle$), three $S^{\mathrm{T}} = 1$ states ($|11\rangle$, $|12\rangle$, and $|13\rangle$), and one $S^{\mathrm{T}} = 2$ state ($|21\rangle$). S^{T} is the magnitude of the sum of the spin operators in the tetramer. The eigenstates $|ij\rangle$ are explicitly given in Ref.[39].

We evaluated the J_1 and J_2 exchange interactions using eigenenergies given in Ref. [39]. Only the set in which $J_1 = 0.74$ meV (8.6 K) and $J_2 = 0.95$ meV (11.0 K) can explain the three excitation energies (0.7, 1.2, and 1.9 meV). The results are shown in Table III. When $J_1 = 0.74$ meV and $J_2 = 0.95$ meV, the ground, first-excited, second-excited, third-excited, fourth-excited, and fifth-excited states (GS, 1ES, 2ES, 3ES, 4ES, and 5ES) are $|02\rangle$, $|13\rangle$, $|11\rangle$, $|01\rangle$, $|12\rangle$, and $|21\rangle$ states, respectively. The 0.7, 1.2, and 1.9 meV excitations

TABLE III: The excitation energy from GS determined experimentally and calculated for the spin tetramer with $J_1 = 0.74$ meV and $J_2 = 0.95$ meV. The excitation from GS to 3ES or 5ES is forbidden (F).

eigenstate	S^{T}	Excitation energy (meV)	
		exp.	calc.
GS $\|02\rangle$	0	0	0
1ES $\|13\rangle$	1	0.7	0.71
2ES $\|11\rangle$	1	1.2	1.22
3ES $\|01\rangle$	0	F	1.68
4ES $\|12\rangle$	1	1.9	1.93
5ES $\|21\rangle$	2	F	2.18

correspond to the excitations from GS to 1ES, 2ES, and 4ES, respectively. The excitations from GS to 3ES and 5ES are forbidden.

We investigated whether the spin tetramer can explain the other results. The solid line in Fig. 2 indicates $\chi(T)$ calculated for the spin tetramer with $J_1 = 0.74$ meV, $J_2 = 0.95$ meV, and $g = 4.2$. We added a constant susceptibility $\chi_0 = 0.01$ (emu/mol Yb). The calculated $\chi(T)$ is close to the experimental $\chi(T)$. The large value of χ_0 is likely attributable to Van Vleck paramagnetism of Yb^{3+} ions. The red solid line in Fig. 3 represents $C_{\mathrm{mag}}(T)$ calculated for the spin tetramer and is consistent with the experimental $C_{\mathrm{mag}}(T)$ at $T < 15$ K. The blue solid line in Fig. 3 indicates $C_{\mathrm{mag}}(T)$ calculated for the spin tetramer when $\mu_0 H = 9$ T and $g = 4.2$, which was used in the calculation of $\chi(T)$. The experimental and calculated $C_{\mathrm{mag}}(T)$ curves corresponding to 9 T are close to each other. We also calculated $\chi(T)$ and $C_{\mathrm{mag}}(T)$ for two isolated dimers with the exchange interactions of 0.7 and 1.2 meV. The dashed line in Fig. 2 indicates the sum of $\chi(T)$ curves of the two dimers and can explain the experimental $\chi(T)$. The dashed line in Fig. 3(a) indicates the sum of $C_{\mathrm{mag}}(T)$ curves at 0 T of the two dimers and is slightly larger than the experimental $C_{\mathrm{mag}}(T)$ at around 4 K. We cannot exclude the two-isolated-dimer model by the results of $\chi(T)$ and $C_{\mathrm{mag}}(T)$. However, the two-isolated-dimer model cannot be applied to Yb_2SiO_5 mainly because of the difference in the intensities at 0.7 and 1.2 meV described in the 2nd paragraph in the section IV.

The experimental and calculated $C_{\mathrm{mag}}(T)$ curves corresponding to 0 T differ with each

other in the temperature range $T > 15$ K. This difference indicates the existence of the CEF excitations. As evident in Fig. 3(b), $S_{\rm mag}(T)$ reaches $R\ln 2$ and $R\ln 4$ at $T \sim 23$ and ~ 150 K, respectively. $R\ln 2$ and $R\ln 4$ correspond to the entropy of the lowest Kramers doublet and that of the lowest and second-lowest Kramers doublets, respectively. We infer that the difference in energy between the lowest and the second-lowest doublets is 100 K (8.62 meV) or larger. Thus, the three excitations at 0.7, 1.2, and 1.9 meV are not CEF excitations. Unfortunately, we could not investigate the CEF excitations using the LTAS because of the small energy transfers.

Next, we consider which spin tetramer can explain the experimental $I(Q)$. The $I(Q)$ curve is given by the formula

$$I(Q) = f(Q)^2\Bigg[A_{12}\left(1-\frac{\sin(Q|\vec{r_1}-\vec{r_2}|)}{Q|\vec{r_1}-\vec{r_2}|}\right)+A_{23}\left(1-\frac{\sin Q|2\vec{r_2}|}{Q|2\vec{r_2}|}\right) \\ +A_{13}\left(1-\frac{\sin(Q|\vec{r_1}+\vec{r_2}|)}{Q|\vec{r_1}+\vec{r_2}|}\right)+A_{14}\left(1-\frac{\sin Q|2\vec{r_1}|}{Q|2\vec{r_1}|}\right)\Bigg]. \quad (3)$$

Each parameter A_{12}, A_{23}, A_{13}, or A_{14} is determined by J_1, J_2, the initial state, and the final state [39]. As shown in Fig. 1(c), the vectors $\vec{r_1}$ and $\vec{r_2}$ denote the positions of $\boldsymbol{S}_1$ and $\boldsymbol{S}_2$, respectively. The values of Yb–Yb pairs are reported in Table II.

Figure 7 shows $I(Q)$ calculated for the six types of spin tetramers. The $I(Q)$ curves from $|02\rangle$ to $|13\rangle$ (from GS to 1ES) and from $|02\rangle$ to $|11\rangle$ (from GS to 2ES) depend on the tetramer, whereas the $I(Q)$ curves from $|02\rangle$ to $|12\rangle$ (from GS to 4ES) are similar to one another. Only the spin tetramer formed by 3NN and 2NN Yb–Yb pairs can explain the experimental $I(Q)$ curves.

The lines in Fig. 6(a) indicate $I(Q)$ calculated for the 3NN–2NN tetramer. The three lines are multiplied by the same value. The experimental $I(Q)$ values at 0.7 and 1.2 meV are consistent with the $I(Q)$ values calculated for the $|02\rangle$ to $|13\rangle$ and $|02\rangle$ to $|11\rangle$ excitations, respectively, when we assume that the background intensity is 74. The isolated spin tetramer model can explain qualitatively the weak intensity of the 1.9 meV excitation. The experimental $I(Q)$ value at 1.9 meV, however, is smaller than the $I(Q)$ value calculated for $|02\rangle$ to $|12\rangle$ excitation even if the background intensity is 0. The lines in Fig. 5(b) indicate $I(T)$ calculated for the 3NN–2NN tetramer. The three lines are multiplied by the same value. The overall T dependence of the experimental curves for the $|02\rangle$ to $|13\rangle$ and $|02\rangle$ to $|11\rangle$ excitations (0.7 and 1.2 meV excitations, respectively) are captured by the present

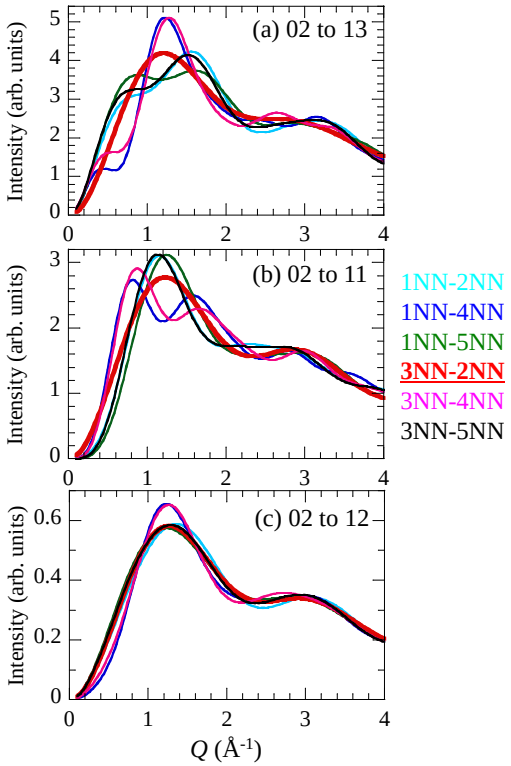

FIG. 7: The Q dependence of the INS intensity $I(Q)$ calculated for the six types of spin tetramers with $J_1 = 0.74$ meV and $J_2 = 0.95$ meV: (a) the excitation from $|02\rangle$ to $|13\rangle$ (from GS to 1ES), corresponding to the 0.7 meV excitation, (b) the excitation from $|02\rangle$ to $|11\rangle$ (from GS to 2ES), corresponding to the 1.2 meV excitation, and (c) the excitation from $|02\rangle$ to $|12\rangle$ (from GS to 1ES), corresponding to the 1.9 meV excitation.

model, while the experimental $I(T)$ value is smaller than the calculated $I(T)$ value for the $|02\rangle$ to $|12\rangle$ excitation.

The spin-1/2 tetramer with $J_1 = 0.74$ meV and $J_2 = 0.95$ meV can explain the excitation energies, $\chi(T)$, and $C_{\rm mag}(T)$ at $T < 15$ K for Yb_2SiO_5. These values are determined by eigenenergies. The $I(Q)$ curves calculated for the $|02\rangle$ to $|13\rangle$ and $|02\rangle$ to $|11\rangle$ excitations are consistent with the experimental $I(Q)$ curves, indicating that the eigenstates are almost correct. However, the spin tetramer cannot well explain the $I(Q)$ at 1.9 meV corresponding to the $|02\rangle$ to $|12\rangle$ excitation and the $I(T)$ value. Probably, weak inter-tetramer interactions affect the eigenstates. The maximum of the half-width at half-maximum (HWHM) at the 0.7 meV excitation is 0.07 meV that is 0.02 meV larger than HWHM of the energy resolution,

suggesting that the maximum of inter-tetramer interactions is 0.02 meV. The experimental and calculated $C_{\rm mag}(T)$ under a 0 T field differ from each other at $T > 15$ K. We will investigate the CEF excitations using INS measurements with higher ω values and will confirm whether CEF-excitation energies can explain $C_{\rm mag}(T)$ at $T > 15$ K.

The spin tetramer is an intriguing spin system. For example, Bose-Einstein condensation of triplons in magnetic fields was found in the spin-1 tetramer antiferromagnet $K_2Ni_2(MoO_4)_3$ [40]. If a magnetic order occurs in spin-tetramer materials, we can expect two types of magnetic excitations such as gapless transverse-mode (Nambu-Goldstone mode) [41] and gapped longitudinal-mode (amplitude Higgs mode) [42] excitations corresponding to fluctuations in directions perpendicular and parallel to ordered moments, respectively [43]. Several spin-tetramer materials have been reported, including CaV_4O_9 ($S = \frac{1}{2}$) [44, 45], Cu_2PO_4 ($S = \frac{1}{2}$) [39], $Cu_2Te_2O_5Br_2$ ($S = \frac{1}{2}$) [46], $Cu_2CdB_2O_6$ ($S = \frac{1}{2}$) [47, 48], $SeCuO_3$ ($S = \frac{1}{2}$) [49], $CuInVO_5$ ($S = \frac{1}{2}$) [50], $Ba_3Yb_2Zn_5O_{11}$ ($S_{\rm eff} = \frac{1}{2}$) [29], and $Rb_2Ni_2(MoO_4)_3$ ($S = 1$) [43]. For some of the materials, the values of J_1, J_2, spin gap, and AFM transition temperature are summarized in Table I in [43]. The J_1 and J_2 values in Yb_2SiO_5 are smaller than those in the materials, reflecting that an exchange interaction in a Yb–Yb pair is usually weak. To our knowledge, Yb_2SiO_5 is the first material based on Yb^{3+} ions with spin tetramers formed by the two types of exchange interactions (*i.e.,* J_1 and J_2 interactions).

Materials based on Yb^{3+} ions have the following advantages when used to investigate spin systems. An exchange interaction between two pseudospins is usually weak, leading to a low energy scale. Phase transitions in magnetic fields can appear even under low magnetic fields. In the Yb^{3+}-based antiferromagnets shown in the Introduction and Yb_2SiO_5, a Yb-Yb length in a Yb-Yb pair where a dominant exchange interaction exists is short as shown in Table I. The length is comparable to that in a pair of two $3d$ ions where a dominant exchange interaction exists. In INS experiments, it is easier to investigate magnetic excitations in a small Q range for Yb^{3+} compounds than for $3d$ compounds. Spin systems formed by Yb^{3+} ions will be studied extensively in the future.

V. CONCLUSION

We investigated the magnetic properties of Yb_2SiO_5 with pseudospins of $S_{\rm eff} = 1/2$ using magnetic susceptibility, specific heat, and INS measurements. A broad maximum

appears at $T_{\rm max} \sim 6$ K in the $\chi(T)$ plot, indicating a low-dimensional AFM spin system. The susceptibility decreases rapidly with decreasing T below $T_{\rm max}$, suggesting a spin-singlet ground state with a spin gap. A maximum was observed at approximately 4 and 8 K in $C_{\rm mag}(T)$ under 0 and 9 T fields, respectively. We observed excitations at $\omega \sim 0.7, 1.2$, and 1.9 meV in INS spectra. The excitations are dispersionless and exist over a wide Q range, indicating cluster excitations. As T is raised, the intensities of the 0.7 and 1.2 meV excitations decrease at $T \leq 30$ K and are almost constant at $T \geq 30$ K. The 1.9 meV excitation is observed only at low temperatures. The T dependence indicates that the three excitations are magnetic in nature. A broad maximum was observed at $Q \sim 1.25$ Å^{-1} in $I(Q)$ for the three excitations, although the Q dependence of the INS intensity is weak at the 1.9 meV excitation. Although a quasi-one-dimensional spin system is expected, the spin system in Yb_2SiO_5 is the $S_{\rm eff} = 1/2$ tetramer formed by the 2NN and 3NN Yb–Yb pairs with $J_1 = 0.74$ meV and $J_2 = 0.95$ meV. The 0.7, 1.2, and 1.9 meV excitations correspond to the excitations from GS to 1ES, 2ES, and 4ES, respectively. The excitations from GS to 3ES and 5ES are forbidden. The isolated spin tetramer model can explain the excitation energies, $\chi(T)$, $C_{\rm mag}(T)$ at $T < 15$ K, and $I(Q)$ at 0.7 and 1.2 meV. This model, however, cannot well explain the $I(Q)$ at 1.9 meV and $I(T)$ for the three excitations, likely because of the effects of weak inter-tetramer interactions.

Acknowledgments

This work was supported by the Japan Society for the Promotion of Science (JSPS) KAKENHI Grant Number 24K06947 and by the World Premier International Research Center Initiative (WPI), Ministry of Education, Culture, Sports, Science and Technology (MEXT), Japan. One of the authors (Naohito Tsujii) has been supported by JSPS KAKENHI (24K00590). This work is partially based on experiments performed on the LTAS (Proposal 2024A-A06) at the JRR-3 reactor, Japan Atomic Energy Agency (JAEA). We thank Manami Ikeda at the National Institute for Materials Science (NIMS) for the sample synthesis and X-ray diffraction measurements. We are grateful to Masamichi Nishino, Kazunari Yamaura, Alexei Belik, and Yoshihiro Tsujimoto at NIMS for their fruitful discussions.

[1] D. C. Johnston, J. W. Johnson, D. P. Goshorn, and A. J. Jacobson, Magnetic susceptibility of $(VO)_2P_2O_7$: A one-dimensional spin-$\frac{1}{2}$ Heisenberg antiferromagnet with a ladder spin configuration and a singlet ground state, Phys. Rev. B **35**, 219 (1987).

[2] A. W. Garrett, S. E. Nagler, D. A. Tennant, B. C. Sales, and T. Barnes, Magnetic Excitations in the $S = 1/2$ Alternating Chain Compound $(VO)_2P_2O_7$, Phys. Rev. Lett. **79**, 745 (1997).

[3] E. Gebert and L. Kihlborg, On the Crystal Structure of Copper Wolframate, Acta Chem. Scand. **21**, 2575 (1967).

[4] B. Lake, D. A. Tennant, R. A. Cowley, J. D. Axe, and C. K. Chen, Magnetic excitations in the ordered phase of the antiferromagnetic alternating chain compound $CuWO_4$, J. Phys.: Condens. Matter **8**, 8613 (1996).

[5] Y. Sasago, M. Hase, K. Uchinokura, M. Tokunaga, and N. Miura, Discovery of a spin-singlet ground state with an energy gap in $CaCuGe_2O_6$, Phys. Rev. B **52**, 3533 (1995).

[6] M. Behruzi, K. H. Breuer, and W. Eysel, Copper(II) silicates and germanates with chain structures. I. $CaCuGe_2O_6$, a strongly deformed pyroxene, Z. Kristallogr. **176**, 205-217 (1986).

[7] C. K. Majumdar and D. K. Ghosh, On next-nearest-neighbor interaction in linear chain .I., J. Math. Phys. **10**, 1388 (1969).

[8] C. K. Majumdar and D. K. Ghosh, On next-nearest-neighbor interaction in linear chain .II., J. Math. Phys. **10**, 1399 (1969).

[9] F. D. M. Haldane, Spontaneous dimerization in the $S = 1/2$ Heisenberg antiferromagnetic chain with competing interactions, Phys. Rev. B **25**, 4925 (1982).

[10] F. D. M. Haldane, Erratum: Spontaneous dimerization in the $S = 1/2$ Heisenberg antiferromagnetic chain with competing interactions, Phys. Rev. B **26**, 5257 (1982).

[11] A. Zheludev, G. Shirane, Y. Sasago, M. Hase, and K. Uchinokura, Dimerized ground state and magnetic excitations in $CaCuGe_2O_6$, Phys. Rev. B **53**, 11642 (1996).

[12] D. A. Tennant, S. E. Nagler, A. W. Garrett, T. Barnes, and C. C. Torardi, Excitation Spectrum and Superexchange Pathways in the Spin Dimer $VODPO_4$-$\frac{1}{2}$ D_2O, Phys. Rev. Lett. **78**, 4998 (1997).

[13] M. Quarton and M. T. Oumba, Proprietes de l' ion Cu^{2+} dans la structure de $AgCuPO_4 - \beta$, Mater. Res. Bull. **18**, 967 (1983).

[14] H. B. Yahia, E. Gaudin, J. Darriet, D. Dai, and M.-H. Whangbo, Comparison of the Crystal Structures and Magnetic Properties of the Low- and High-Temperature Forms of $AgCuPO_4$: Crystal Structure Determination, Magnetic Susceptibility Measurements, and Spin Dimer Analysis, Inorg. Chem. **45**, 5501 (2006).

[15] M. Hase, M. Matsuda, K. Kakurai, K. Ozawa, H. Kitazawa, N. Tsujii, A. Dönni, and H. Kuroe, Inelastic neutron scattering study of the spin-gap cuprate β-$AgCuPO_4$, Phys. Rev. B **76**, 134403 (2007).

[16] R. Kumar, K. Nam, S.-H. Kim, K. H. Kim, and A. Sundaresan, Exploring potential quantum spin liquid state in a quasi-one-dimensional magnetic chain, Phys. Rev. B **109**, 224429 (2024).

[17] L. S. Wu, S. E. Nikitin, M. Brando, L. Vasylechko, G. Ehlers, M. Frontzek, A. T. Savici, G. Sala, A. D. Christianson, M. D. Lumsden, and A. Podlesnyak, Antiferromagnetic ordering and dipolar interactions of $YbAlO_3$, Phys. Rev. B **99**, 195117 (2019).

[18] Y. Li, H. Liao, Z. Zhang, S. Li, F. Jin, L. Ling, L. Zhang, Y. Zou, L. Pi, Z. Yang, J. Wang, Z. Wu, and Q. Zhang, Gapless quantum spin liquid ground state in the two dimensional spin-1/2 triangular antiferromagnet $YbMgGaO_4$, Sci. Rep. **5**, 16419 (2015).

[19] Y. Li, G. Chen, W. Tong, L. Pi, J. Liu, Z. Yang, X. Wang, and Q. Zhang, Rare-Earth Triangular Lattice Spin Liquid: A Single-Crystal Study of $YbMgGaO_4$, Phys. Rev. Lett. **115**, 167203 (2015).

[20] Y. Shen, Y.-D. Li, H. Wo, Y. Li, S. Shen, B. Pan, Q. Wang, H. C. Walker, P. Steffens, M. Boehm, Y. Hao, D. L. Quintero-Castro, L. W. Harriger, M. D. Frontzek, L.e Hao, S. Meng, Q. Zhang, Gang Chen, and J. Zhao, Evidence for a spinon Fermi surface in a triangular lattice quantum-spin-liquid candidate, Nature **540**, 559 (2016).

[21] F. L. Pratt, F. Lang, W. Steinhardt, S. Haravifard, and S. J. Blundell, Spin dynamics, entanglement, and the nature of the spin liquid state in $YbZnGaO_4$, Phys. Rev. B **106**, L060401 (2022).

[22] K. Somesh, S. S. Islam, S. Mohanty, G. Simutis, Z. Guguchia, Ch. Wang, J. Sichelschmidt, M. Baenitz, and R. Nath, Absence of magnetic order and emergence of unconventional fluctuations in the $J_{\text{eff}} = \frac{1}{2}$ triangular-lattice antiferromagnet $YbBO_3$, Phys. Rev. B **107**, 064421 (2023).

[23] K. M. Nuttall, C. Z. Suggs, H. E. Fischer, M. M. Bordelon, S. D. Wilson, and B. A. Frandsen, Quantitative investigation of the short-range magnetic correlations in the candidate quantum spin liquid $NaYbO_2$, Phys. Rev. B **108**, L140411 (2023).

[24] Z. Zhang, Y. Cai, J. Kang, Z. Ouyang, Z. Zhang, A. Zhang, J. Ji, F. Jin, and Q. Zhang, Anisotropic exchange coupling and ground state phase diagram of Kitaev compound YbOCl, Phys. Rev. Research **4**, 033006 (2022).

[25] G. Sala, M. B. Stone, B. K. Rai, A. F. May, D. S. Parker, G. B. Halász, Y. Q. Cheng, G. Ehlers, V. O. Garlea, Q. Zhang, M. D. Lumsden, and A. D. Christianson, Crystal field splitting, local anisotropy, and low-energy excitations in the quantum magnet $YbCl_3$, Phys. Rev. B **100**, 180406(R) (2019).

[26] J. Xing, E. Feng, Y. Liu, E. Emmanouilidou, C. Hu, J. Liu, D. Graf, A. P. Ramirez, G. Chen, H. Cao, and N. Ni, Néel-type antiferromagnetic order and magnetic field-temperature phase diagram in the spin-$\frac{1}{2}$ rare-earth honeycomb compound $YbCl_3$, Phys. Rev. B **102**, 014427 (2020).

[27] G. Hester, H. S. Nair, T. Reeder, D. R. Yahne, T. N. DeLazzer, L. Berges, D. Ziat, J. R. Neilson, A. A. Aczel, G. Sala, J. A. Quilliam, and K. A. Ross, Novel Strongly Spin-Orbit Coupled Quantum Dimer Magnet: $Yb_2Si_2O_7$, Phys. Rev. Lett. **123**, 027201 (2019).

[28] S. Mohanty, S. S. Islam, N. Winterhalter-Stocker, A. Jesche, G. Simutis, Ch. Wang, Z. Guguchia, J. Sichelschmidt, M. Baenitz, A. A. Tsirlin, P. Gegenwart, and R. Nath, Disordered ground state in the spin-orbit coupled $J_{\text{eff}} = \frac{1}{2}$ distorted honeycomb magnet $BiYbGeO_5$, Phys. Rev. B **108**, 134408 (2023).

[29] K. Kimura, S. Nakatsuji, and T. Kimura, Experimental realization of a quantum breathing pyrochlore antiferromagnet, Phys. Rev. B **90**, 060414(R) (2014).

[30] M. Pula, S. Sharma, J. Gautreau, K. P. Sajilesh, A. Kanige, M. D. Frontzek, T. N. Dolling, L. Clark, S. Dunsiger, A. Ghara, and G. M. Luke, Candidate for a quantum spin liquid ground state in the Shastry-Sutherland lattice material $Yb_2Be_2GeO_7$, Phys. Rev. B **110**, 014412 (2024).

[31] J. Khatua, S. Bhattacharya, Q. P. Ding, S. Vrtnik, A. M. Strydom, N. P. Butch, H. Luetkens, E. Kermarrec, M. S. Ramachandra Rao, A. Zorko, Y. Furukawa, and P. Khuntia, Spin liquid state in a rare-earth hyperkagome lattice, Phys. Rev. B **106**, 104404 (2022).

[32] B. Sana, M. Barik, M. Pregelj, U. Jena, M. Baenitz, J. Sichelschmidt, K. Sethupathi, and P. Khuntia, Magnetic properties of a spin-orbit entangled $J_{\text{eff}} = \frac{1}{2}$ three-dimensional frustrated rare-earth hyperkagome material, Phys. Rev. B **108**, 134413 (2023).

[33] G. Buisson and C. Michel, An isomorphic series of rare earth orthosilicates (T_2SiO_5) and

orthogermanates (T_2GeO_5), Mater. Res. Bull. **3**, 193 (1968).

[34] Y. I. Smolin, Crystal structure of ytterbium oxyorthosilicate Yb_2SiO_5, Sov. Phys. Crystallogr. **14**, 854 (1970) [Kristallografiya **14**, 985 (1969)].

[35] G. V. Ananeva, A. M. Korovkin, T. I. Merkulyaeva, A. M. Morozova, M. V. Petrov, I. R. Savinova, V. R. Startsev, P. P. Feofilov, Growth of lanthanide oxyorthosilicate single-crystals, and their structural and optical characteristics, Inorg. Mater. **17**, 754 (1981) [Izv. Akad. Nauk SSSR, Neorg. Mater. **17**, 1037 (1981)].

[36] K. Momma and F. Izumi, VESTA for three-dimensional visualization of crystal, volumetric and morphology data, J. Appl. Cryst. **44**, 1272 (2011).

[37] K. Kaneko, C. Tabata, M. Hagihala, H. Yamauchi, Y. Oba, T. Kumada, M. Kubota, Y. Kojima, N. Nabatame, M. Sasaki, Y. Shimojo, K. Kodama, and T. Osakabe, New Standard for Low Temperature Sample Environment at JAEA/JRR-3, JPS Conf. Proc. **41**, 011015 (2024).

[38] P. J. Brown, Magnetic form factors, International Tables for Crystallography Vol. **C**, Section 4.4.5, 454 (2006).

[39] M. Hase, K. M. S. Etheredge, S.-J. Hwu, K. Hirota, and G. Shirane, Spin-singlet ground state with energy gaps in Cu_2PO_4: Neutron-scattering, magnetic-susceptibility, and ESR measurements, Phys. Rev. B **56**, 3231 (1997). In this reference, the Hamiltonian is defined as $\mathcal{H} = \sum_{i,j} 2J_{ij} S_i \cdot S_j$ instead of $\mathcal{H} = \sum_{i,j} J_{ij} S_i \cdot S_j$ in the present paper.

[40] B. Koteswararao, P. Khuntia, R. Kumar, A. V. Mahajan, A. Yogi, M. Baenitz, Y. Skourski, and F. C. Chou, Bose-Einstein condensation of triplons in the $S = 1$ tetramer antiferromagnet $K_2Ni_2(MoO_4)_3$: A compound close to a quantum critical point, Phys. Rev. B **95**, 180407(R) (2017).

[41] J. Goldstone, A. Salam, and S. Weinberg, Broken symmetries, Phys. Rev. **127**, 965 (1962).

[42] P. W. Higgs, Broken Symmetries and the Masses of Gauge Bosons, Phys. Rev. Lett. **13**, 508 (1964).

[43] M. Hase, A. Matsuo, K. Kindo, and M. Matsumoto, Magnetism of the spin-1 tetramer compound $A_2Ni_2MO_3O_{12}$ (A = Rb or K) ($S = 1$), Phys. Rev. B **96**, 214424 (2017).

[44] S. Taniguchi, T. Nishikawa, Y. Yasui, Y. Kobayashi, M. Sato, T. Nishioka, M. Kontani, and K. Sano, Spin Gap Behavior of $S = 1/2$ Quasi-Two-Dimensional System CaV_4O_9 J. Phys. Soc. Jpn. **64**, 2758 (1995).

[45] N. Katoh and M. Imada, Spin gap in two-dimensional Heisenberg model for CaV_4O_9 J. Phys. Soc. Jpn. **64**, 4105 (1995).

[46] P. Lemmens, K.-Y. Choi, E. E. Kaul, C. Geibel, K. Becker, W. Brenig, R. Valenti, C. Gros, M. Johnsson, P. Millet, and F. Mila, Evidence for an Unconventional Magnetic Instability in the Spin-Tetrahedra System $Cu_2Te_2O_5Br_2$ ($S = \frac{1}{2}$), Phys. Rev. Lett. **87**, 227201 (2001).

[47] M. Hase, A. Dönni, V. Yu. Pomjakushin, L. Keller, F. Gozzo, A. Cervellino, and M. Kohno, Magnetic structure of $Cu_2CdB_2O_6$ exhibiting a quantum-mechanical magnetization plateau and classical antiferromagnetic long-range order, Phys. Rev. B **80**, 104405 (2009).

[48] M. Hase, K. Nakajima, S. Ohira-Kawamura, Y. Kawakita, T. Kikuchi, and M. Matsumoto, Magnetic excitations in the spin-$\frac{1}{2}$ tetramer substance $Cu_2^{114}Cd^{11}B_2O_6$ obtained by inelastic neutron scattering experiments, Phys. Rev B **92**, 184412 (2015).

[49] I. Živković, D. M. Djokić, M. Herak, D. Pajić, K. Prša, P. Pattison, D. Dominko, Z. Micković, D. Cinčić, L. Forró, H. Berger, and H. M. Rønnow, Site-selective quantum correlations revealed by magnetic anisotropy in the tetramer system $SeCuO_3$, Phys. Rev. B **86**, 054405 (2012).

[50] M. Hase, M. Matsumoto. A. Matsuo, and K. Kindo, Magnetism of the antiferromagnetic spin-$\frac{1}{2}$ tetramer compound $CuInVO_5$, Phys. Rev. B **94**, 174421 (2016).